Low-Frequency Extragalactic Radio Point Source Samples: A Review Postprint

Authors: Lin Jinyang, Zhu Zhenghao, Ma Renyi

Date: 2025-10-10T00:00:00+00:00

Abstract

Low-frequency radio point sources are of significant importance in astronomical research, as they not only play a crucial role in studying galaxy evolution history, but also constitute the primary foreground contamination source for detecting signals from the Epoch of Reionization. Low-frequency observations are essential for studying and understanding the properties of radio point sources. This paper introduces the radiation mechanisms of radio point sources and current observational catalogs of low-frequency radio point sources, which play an important role in research on the classification, redshift distribution, flux distribution, luminosity function, and spectral index of radio point sources. Furthermore, it provides a detailed introduction to the main radio point source simulation software, their simulation methods, and the radio point source catalogs they generate. These software and data hold significant value for in-depth understanding of the statistical properties and cosmological implications of radio point sources.

Full Text

Preamble

Vol. 43, No. 3
Sept., 2025

PROGRESS IN ASTRONOMY
doi: 10.3969/j.issn.1000-8349.2025.03.03

Review of Low-Frequency Extragalactic Radio Point Source Catalogs

LIN Jinyang[1], ZHU Zhenghao[2], MA Renyi[1]
(1. College of Physical Science and Technology, Xiamen University, Xiamen 361005, China;
2. Shanghai Astronomical Observatory, Chinese Academy of Sciences, Shanghai 200030, China)

Abstract

Low-frequency radio point sources are of great significance in astronomical research, playing a crucial role in studying galaxy evolution while also serving as the primary foreground contaminant for detecting signals from the Epoch of Reionization. Low-frequency observations are essential for understanding the properties of radio point sources. This paper introduces the radiation mechanisms of radio point sources and reviews current low-frequency radio point source catalogs, which are important for investigating source classification, redshift distribution, flux distribution, luminosity functions, and spectral indices. Additionally, we provide detailed descriptions of major radio point source simulation software, their simulation methods, and the resulting radio point source catalogs. These software tools and data are valuable for gaining deeper insights into the statistical properties and cosmological implications of radio point sources.

Keywords: radio galaxies; active galactic nuclei; catalogs
CLC number: P161.4
Document code: A

1 Introduction

Radio astronomy, as an important branch of astronomy, primarily studies celestial objects and cosmic phenomena through observations of radio waveband radiation. Limited by atmospheric windows, our observable frequency range is 10 MHz–1 THz. Although the atmospheric window permits observations down to 10 MHz, technological constraints have historically concentrated radio research and observations at frequencies above 1 GHz. Compared to mid- and high-frequency bands, low-frequency bands offer several advantages, such as detecting neutral hydrogen 21 cm radiation from the Epoch of Reionization (EoR), which after significant redshifting appears in the low-frequency radio band of 50–200 MHz. Conducting EoR signal detection experiments in this band is of great importance. Additionally, longer wavelengths at lower frequencies are less affected by dust, making it easier to observe the central regions of galaxies.

Radiation in the low-frequency band is dominated by synchrotron radiation—emission produced by high-energy charged particles accelerating in magnetic fields. Synchrotron radiation is brighter and longer-lived at low frequencies, facilitating the detection and study of diffuse radio emission from galaxy clusters, superclusters, and large-scale filamentary structures. Moreover, since the strength of various plasma effects (such as scattering, dispersion, and Faraday rotation) scales as $^{-2}$, low-frequency bands are better suited for studying interstellar magnetic field distributions and electron density. Low-frequency radio telescopes typically have larger fields of view, significantly increasing survey speed and facilitating the search for pulsars and transients.

In low-frequency radio observations and research, the study of extragalactic radio point sources is an extremely important component. To understand galaxy

formation and evolution, we need to comprehend how baryons drive and suppress star formation. Radio observations provide an important window for this, as they directly reveal three key populations: star-forming galaxies (SFGs), radio-loud active galactic nuclei (RLAGN), and radio-quiet active galactic nuclei (RQ-AGN). These radio point sources are also important foreground contaminants for EoR signal detection, contributing 27% of the total foreground contamination at 150 MHz. On small angular scales of the power spectrum, extragalactic point sources become the strongest and most difficult foreground component to handle. Radio point sources are also crucial for interferometric array calibration, where flux calibration is typically achieved by observing a bright source with known flux density and solving for antenna gains that are then transferred to target source data. Calibration sources are selected from those with precisely known flux densities that vary slowly with time. In the northern hemisphere, 3C48, 3C138, 3C147, and 3C286 are commonly used as calibration sources. For phase calibration, especially when affected by the ionosphere, frequent switching to nearby calibrators is required, with the maximum distance between target and calibrator limited by coherence time and isoplanatic patch size.

With advances in observational technology and telescope capabilities, we are detecting increasing numbers of radio point sources. Current major low-frequency radio point source catalogs include: the Murchison Widefield Array (MWA) Galactic and Extragalactic All-sky MWA Survey (GLEAM) low-frequency point source catalog, the LOFAR Two-metre Sky Survey (LoTSS) low-frequency point source catalog from the Low Frequency Array (LOFAR) in the northern sky, the 21CMA extragalactic point source catalog, and several low-frequency catalogs obtained through cross-matching with optical/infrared galaxy catalogs. These catalogs provide crucial support for studying various properties of radio point sources, such as radio spectra, redshift distribution, and luminosity functions of extragalactic sources.

In extragalactic point source research, radio point source sky simulation is a useful tool for evaluating survey completeness or predicting the number of sources to be observed in future surveys. Current major simulation tools include SKADS (Square Kilometre Array Design Study) and T-RECS (Tiered Radio Extragalactic Continuum Simulation). To ensure consistency with real observations, these simulation programs are designed based on modeling information from extensive radio point source catalogs.

This paper systematically introduces radio point sources and their catalogs to support research in this field. Section 2 describes the radiation mechanisms of radio point sources. Section 3 introduces low-frequency radio point source observation catalogs. Section 4 presents radio point source simulation software and their generated catalogs. Section 5 summarizes the paper and provides an outlook for future observations and simulations.

2 Radiation Mechanisms of Radio Point Sources

In the low-frequency radio band, the dominant radiation mechanism for extragalactic point sources is synchrotron radiation, with supernova remnants and processes related to supermassive black holes being the main sources of synchrotron radiation in galaxies. Synchrotron radiation is produced when charged particles move at relativistic speeds in magnetic fields. For relativistic electrons, due to Doppler effects, the radiation is highly directional, concentrated within a narrow cone of half-angle γ^{-1} around the direction of the electron' s helical motion tangential velocity, where γ is the Lorentz factor representing the ratio of particle energy to its rest energy.

We present here the spectral distribution of synchrotron radiation from a single relativistic electron, with detailed derivations available in Section 2.7 of reference [22]:

$$P(\nu)d\nu = \frac{3e^{3B}\sin\alpha}{4\pi\epsilon_{0c}}F(x)d\nu$$

where is the frequency, B is the magnetic field strength, and α is the pitch angle of the electron' s helical motion. The function F(x) contains the spectral shape and involves an integral of modified Bessel functions of order 5/3: F(x) x $x\hat{}\infty$ $K\{5/3\}(\ )$ d . Considering the polarization properties of synchrotron radiation, we decompose the emission into components perpendicular and parallel to the magnetic field, involving the function G(x) x $x\hat{}\infty$ $K\{2/3\}(\ )$ d . The power spectra for the two polarization components are:

$$P_{\perp,\parallel}(\nu) = \frac{e^{3B}\sin\alpha}{8\pi\epsilon_{0c}}\begin{cases} F(x)+G(x) & (\perp B) \\ F(x)-G(x) & (\parallel B) \end{cases}$$

The linear polarization degree of synchrotron radiation is:

$$\Pi(\nu) = \frac{P_\perp(\nu)-P_\parallel(\nu)}{P_\perp(\nu)+P_\parallel(\nu)} = \frac{G(x)}{F(x)}$$

For most cases, the linear polarization degree of synchrotron radiation is between 0.70 and 0.75, making strong linear polarization a characteristic feature.

We consider a relativistic gas with energy number density distribution N_E and assume an isotropic pitch angle distribution: dN_E = CE$\hat{}${-p}dE, where p is the spectral index and C is a constant. The energy distribution of cosmic rays and radiating electrons in many other synchrotron sources follows a power-law form. Convolving the electron energy distribution with the synchrotron spectrum of a single electron, the spectral emissivity (radiated power per unit volume, per unit solid angle, per unit frequency interval) for a power-law distribution with isotropic pitch angles can be written in closed form. The function

a(p) (see Table 1) is typically used to simplify the dependence of spectral emissivity on the power-law spectral index. For typical cases encountered in radio astronomy, a(p) is generally on the order of 10^{-1}. The spectral emissivity for electrons with spectral index p, isotropic pitch angle distribution, and power-law energy distribution is [22]:

$$j_\nu = \frac{3^{(p+1)/2}}{8\pi}\left(\frac{e}{4\pi\epsilon_{0mc}^2}\right)^{(p-1)/2} CB^{(p+1)/2}\nu^{-(p-1)/2}a(p)$$

Table 1 Values of the a(p) function for energy spectral index p [46]

For optically thin sources, radiation intensity can be obtained by integrating the spectral emissivity along the line of sight. For a source with uniform density and path length L along the line of sight, integration yields the radiation intensity [22]:

$$I_\nu = 1.35 \times 10^{-25} CB^{(p+1)/2}\left(\frac{\nu}{6.26 \times 10^{18}}\right)^{-(p-1)/2} a(p)L$$

where I_ has units of $\mathrm{W \cdot m^{-2} \cdot sr^{-1} \cdot Hz^{-1}}$.

It is evident that synchrotron radiation from relativistic electrons with a power-law energy distribution also follows a power-law spectrum: dN_E E^{-} , I_ $^{-(\ -1)}/^{2}$. For most extragalactic radio point sources, since their radiation is dominated by synchrotron emission, their flux density S_ also follows a power-law spectrum: S_ $^{-}$, where α = (p - 1)/2 is the spectral index. Most radio galaxies or quasars have spectral indices in the range of -2 to 0. This power-law spectrum does not extend indefinitely to lower frequencies; under certain physical conditions, the source becomes opaque to its own synchrotron radiation, causing the spectrum to bend—a phenomenon known as synchrotron self-absorption [22].

When a relativistic electron gas is surrounded by a uniform magnetic field, electrons of all energies produce linearly polarized radiation. The linear polarization degree for a gas with a power-law energy distribution with spectral index p can be obtained by integrating the single-electron polarization analysis (Equation (3)) over all energies and pitch angles:

$$\Pi = \frac{p+1}{p+7/3}$$

For a typical energy spectral index p = 2.5, the resulting linear polarization degree is about 0.72, close to the value for a single electron. In practice, observed radiation is the sum over different regions of non-uniform magnetic fields, and superposition effects along and perpendicular to the line of sight within the observing beam can significantly reduce the polarization degree.

The radiation mechanisms of extragalactic point sources mainly include synchrotron radiation, free-free radiation, and thermal radiation, with synchrotron radiation dominating at low frequencies [22]; while at frequencies 30 GHz, free-free radiation becomes dominant [45]. Additionally, since different types of extragalactic point sources have different radiation patterns, classification is important. In current extragalactic radio surveys, it is generally believed that extragalactic point sources are primarily composed of star-forming galaxies and active galactic nuclei [45, 47, 48].

Star-forming galaxies are relatively weak radio sources, typically dominating at lower radio flux density ranges [40, 49], such as below 1 mJy at 150 MHz [31]. The synchrotron radiation in star-forming galaxies is produced by relativistic plasma accelerated in supernova remnants associated with massive (M 8M) star formation [45]; therefore, radio observations can probe recent star formation activity and trace its location to some extent, which has led to the confirmation of the far-infrared–radio correlation. In star-forming galaxies, infrared and radio radiation show a strong linear correlation [50]. Currently, there are two main modes of star formation: starburst mode, possibly triggered by galaxy mergers or high-density star-forming regions, and a more normal mode associated with long-term star formation processes. Observations show that most star-forming galaxies are in the second mode [51]. For this mode, the star formation rate (SFR) is strongly correlated with stellar mass M* [52–54], a relationship that can be described by a power law: SFR M*$^\wedge\beta$ ($\beta = 0.4$–1). Such star-forming galaxies are generally considered to lie on the star-forming main sequence.

The fundamental characteristic of active galactic nuclei is that their energy originates from the relativistic deep potential well of a supermassive black hole at the galaxy center [55]. AGN have various complex classification schemes, with frequent overlap between subclasses from different classification methods. We now introduce the main classifications of AGN.

Based on the primary mode of energy output, AGN can be divided into radiative-mode and jet-mode AGN [55, 56], with structures shown in Figure 1

. Radiative-mode AGN primarily release energy through electromagnetic radiation, while jet-mode AGN produce relatively little electromagnetic radiation, instead transporting large amounts of kinetic energy through concentrated jets on both sides. These jets may be driven by gas accretion onto the supermassive black hole or by its spin energy. In the past, jet-mode AGN were generally classified as low-excitation radio galaxies.

Figure 1 Radiative-mode and jet-mode active galactic nuclei [55]

The basic structure of radiative-mode AGN consists of a supermassive black hole surrounded by a geometrically thin, optically thick accretion disk that extends to the radius of the innermost stable orbit around the central black hole. These systems have high radiative power that ionizes gas clouds in both the broad-line and narrow-line regions. Additionally, they possess a dusty gas obscuring structure that prevents direct observation of the accretion disk and

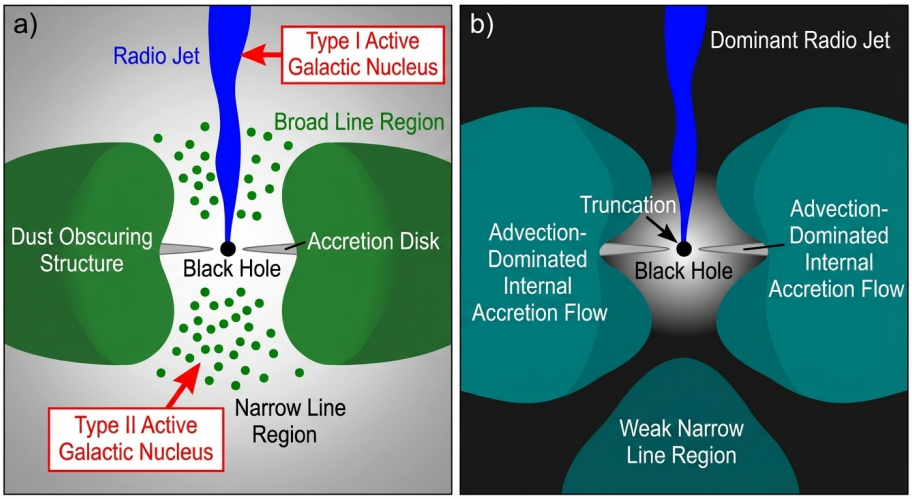

Figure 1: Figure 1

broad-line region from certain directions. Jet-mode AGN, by contrast, have their thin accretion disk replaced in the inner region by a geometrically thick gas accretion flow, which may transition to a truncated thin disk at larger radii. Their lower radiative power can only ionize gas clouds in the narrow-line region.

When observing AGN from near the polar axis of the obscuring structure, the supermassive black hole, accretion disk, corona, and broad-line region can be clearly seen; these are generally called Type I AGN. When observed from near the equatorial plane of the obscuring structure, the central region cannot be seen; these are called Type II AGN. This is the standard unification model for radiative-mode AGN, which posits that the difference between Type I and Type II AGN is solely due to viewing angle. The existence of Type II AGN can still be inferred through thermal infrared radiation from the obscuring structure, hard X-rays propagating through it, or characteristic emission line ratios from the narrow-line region [55].

Jet-mode AGN exhibit a unique supermassive black hole accretion mode showing lower radiative and accretion rates. Their geometrically thin disk may be absent or truncated by a geometrically thick structure where the gas inflow timescale is shorter than the radiative cooling timescale [57–61]; this is called advection-dominated or radiatively inefficient accretion flow. A typical feature of these flows is their ability to emit bilateral jets [55]. For jet-mode AGN, accretion rates are typically below 1% of the Eddington rate, while for radiative-mode AGN, typical accretion rates are 1%–10% of the Eddington rate.

Based on radio morphology—specifically the ratio between the extent of the lowest surface brightness contour and the distance between the brightest regions on either side of the central galaxy—AGN can be classified as FRI (ratio <

0.5) or FRII (ratio $>$ 0.5) [62]. FRII sources have prominent hotspots and bright outer edges, while FRI sources show more diffuse radio emission. Generally, low-accretion-rate sources produce weaker jets and exhibit FRI structure, while higher-accretion-rate galaxies produce stronger jets and show FRII structure [55]. Radio source morphology may also be influenced by environment, as sources in dense regions are more likely to show FRI shapes, possibly because jets are more easily disrupted in such regions [63]. A third class, FR0, has recently been proposed [64], which has FRI characteristics but lacks obvious extended radio emission [47].

As previously mentioned, synchrotron radiation dominates radio point source emission, so most AGN spectra follow a power-law form. Based on spectral index α, radio point sources can be divided into flat-spectrum sources ($\alpha <$ 0.5) and steep-spectrum sources ($\alpha \geq 0.5$) [65-68]; $\alpha = 0.5$ can also serve as an approximate boundary between extended and point sources [69]. Flat-spectrum radio sources have two subclasses: flat-spectrum radio quasars (FSRQs) and BL Lacertae objects (BL Lacs). In optical spectra, FSRQs show strong, broad emission lines like standard quasars, while BL Lacs show at most weak emission lines, sometimes absorption lines, and in many cases no features at all [47].

The most common classification divides AGN into radio-loud and radio-quiet [70–73]. The main physical difference is the presence or absence of strong relativistic jets [47]. Current classification criteria include: (1) dividing based on radio flux density or radio luminosity [74], with the luminosity standard at 1.4 GHz being $L_{1\cdot4}\mathrm{GHz} = 10^{23}$ W $\cdot$ Hz^{-1} [22], though some propose $L_{1\cdot4}\mathrm{GHz} = 7 \times 10^{24}$ W $\cdot$ Hz^{-1} [75], with differences possibly related to the redshift range of the selected sample [17]; and (2) dividing based on the ratio of radio to optical flux density or luminosity [76]. These two types are fundamentally different objects: radio-loud AGN release most of their energy non-thermally (through synchrotron radiation) and are associated with powerful relativistic jets, while radio-quiet AGN have multi-wavelength radiation dominated by thermal processes related directly or indirectly to the accretion disk [17, 47, 77]. Radio-quiet AGN may also have active nuclei that contribute partially to their radio emission [78, 79]. They show clear signs of nuclear activity in non-radio bands (X-ray, mid-infrared, optical) but lack evidence for large-scale radio jets, and their radio emission is much weaker than that of radio-loud AGN [17, 70]. The mechanism of radio emission in radio-quiet AGN remains controversial. Current observational indications suggest two possible origins: star formation and active nuclei. On one hand, radio-quiet AGN have infrared-to-radio flux ratios, evolving luminosity functions, host galaxy colors, optical morphology, and stellar masses similar to star-forming systems [49, 51], suggesting star formation dominates their radio emission [70, 80, 81]. On the other hand, some studies find radio-quiet AGN show higher radio brightness compared to star-forming galaxies of similar mass [73, 82]. These differing findings may result from samples probing different luminosity and redshift ranges [72]. Proposed models for radio emission in radio-quiet AGN include star formation activity like in star-forming galaxies [83], mini-jets [84], coronae [85], and disk winds [86].

Finally, based on optical spectral features, AGN can be classified as high-excitation or low-excitation radio galaxies. High-excitation radio galaxy spectra contain strong emission lines such as [OII]$ 3727, $[OIII]$ 5007, and[NeII]$ 3867, $whilelow-excitationradiogalaxyspectrashowabsorptionlinesorweaker$[OII]$ 3727$emission$[87].Thisclassificationhasbe Å line [88] or high/low excitation or ionization emission lines as criteria [89, 90, 90–92]. Generally, AGN with high-level emission lines in their optical spectra are called high-excitation radio galaxies, and vice versa for low-excitation radio galaxies. High-excitation radio galaxies are primarily driven by efficient accretion of cold gas onto geometrically thin, optically thick accretion disks [93, 94], with accretion rates typically 1%–10% of the Eddington rate [95], producing highly excited emission lines. Low-excitation radio galaxies are more often fueled by accretion of warm gas from the intergalactic medium onto geometrically thick disks, with accretion rates generally below 1% of the Eddington rate [95]; they typically do not show X-ray radiation associated with the accretion process [96] nor infrared radiation from the AGN torus [94, 97].

The different AGN classifications described above overlap to some extent. For example, radiative-mode AGN include high-excitation radio galaxies, while jet-mode AGN are called low-excitation radio galaxies [55]. Nearly all FRI sources are low-excitation radio galaxies, while most FRII sources with strong emission lines are classified as high-excitation radio galaxies. However, FRI and FRII do not perfectly correspond to low- and high-excitation radio galaxies, as some (20%) FRII sources have been shown to be low-excitation radio galaxies [63]. Compared to FRII or high-excitation radio galaxies, FRI or low-excitation radio galaxies have less obscuration of their central regions, suggesting they may lack a dusty torus or have a non-standard geometrically thick ring [47, 98, 99].

3 Low-Frequency Radio Point Source Observation Catalogs

With increasing numbers of low-frequency radio point source observations, catalogs have become more complete in terms of redshift, flux, sky coverage, and brightness completeness analysis. Studying radio point source samples provides clearer understanding of their properties, spatial distribution (clustering), luminosity functions, and size models, while also aiding research on foreground contamination in EoR signal detection.

This chapter introduces low-frequency radio point source catalogs. Table 2 summarizes key information for the extragalactic point source catalogs discussed below: catalog name, frequency, sky area, redshift information, source classification (e.g., AGN vs. star-forming galaxies), and completeness information.

Table 2 Summary of extragalactic point source catalog information

Extragalactic Point Source Catalog	Frequency Range	Sky Area	Number of Sources	Source Classification	Redshift	Completeness
GLEAM-I	72–231 MHz					
GLEAM-II	72–231 MHz					
GLEAM-III	72–231 MHz					
LoLSS	42–66 MHz					
LoTSS-DR1	120–168 MHz					
LoTSS-DR2	120–168 MHz					
LoTSS-DP-DR1	75–175 MHz					
21CMA-NCP	72–231 MHz					
VLSSr						
T-RaMiSu						
GLEAM-6dFGS						

3.1 GLEAM

The GLEAM-I low-frequency extragalactic point source catalog was calibrated using MWA telescope survey data from the first year (2013–2014) of observations [23]. The catalog covers 24,831 square degrees of sky south of declination +30° and outside the Galactic plane $±$10°, containing 307,455 radio sources. The observed flux density frequency range covers 72–231 MHz with 8 MHz bandwidth. To study completeness at different flux levels, 25,000 simulated sources with flux densities of 25 mJy–1 Jy were inserted into the images and identified using the same method. At 200 MHz, the sample achieves 90% completeness at 170 mJy and 50% completeness at 55 mJy. The catalog also assessed its reliability by identifying negative-flux sources (image artifacts near bright sources caused by calibration and deconvolution errors) and determined a reliability of 99.97% based on the ratio of negative to total sources.

The catalog fitted spectral indices (S $\hat{}$ α) for all 245,470 sources with positive flux densities in each frequency sub-band and statistically analyzed the distribution across different flux ranges. At 200 MHz, the median spectral index is -0.78 ± 0.20 for 122,959 sources with flux density < 0.16 Jy, -0.79 ± 0.15 for 86,548 sources with 0.16–0.5 Jy, -0.83 ± 0.12 for 20,606 sources with 0.5–1.0 Jy, and -0.83 ± 0.11 for 12,723 sources with > 1.0 Jy. These provide rich information on low-frequency radio point source spectral index distributions [23]. The catalog

also statistically analyzed the flux distribution in low-noise regions (0h < RA < 3h and -60° < Dec < -10°; 10h < RA < 12h and -40° < Dec < -15°, with average noise of 6.8 ± 1.3 mJy) and compared results with other observations, as shown in Figure 2.

As a supplement to GLEAM-I, the GLEAM-II low-frequency point source catalog covers 2,860 square degrees of sky in the Galactic plane region with $|b| \leq 10°$, Galactic longitude 345°–67° and 180°–240° [24]. Compared to GLEAM-I, GLEAM-II used the multi-scale CLEAN feature of WSCLEAN [108] to better deconvolve large-scale Galactic structures. This supplementary catalog contains 22,037 radio point sources and was analyzed using the same method as GLEAM-I, achieving 50% completeness at 120 mJy at 200 MHz and 99.86% reliability. The catalog also fitted spectral indices for sources in this region, finding that 17,244 sources have power-law spectral energy distributions. At 200 MHz, the median spectral index is -0.89 for sources with flux density < 0.16 Jy, -0.86 for 0.16–0.5 Jy, -0.88 for 0.5–1.0 Jy, and -0.87 for > 1.0 Jy [24]. Finally, 5,749 sources in this catalog are resolved (integrated-to-peak flux density ratio > 1.1), with 168 showing obvious extension (ratio > 2).

GLEAM-III uses MWA telescope survey data from the first two years (2013–2015). This low-frequency point source catalog is centered on the south Galactic pole (SGP), covering 5,113 square degrees from declination -48° to -2° and right ascension 20h40min to 05h04min, totaling 108,851 radio point sources. Compared to GLEAM-I, GLEAM-III has longer integration time, better uv-coverage, and improved processing, reducing the sky RMS noise by 40% in the observed region. Instead of using calibration source observations, GLEAM-III used GLEAM-I as the sky model for calibration. The catalog fitted spectra for 77% of sources, measuring a mean and median spectral index of -0.81 and -0.82 for 83,328 sources. By modeling the relationship between integrated-to-peak flux density ratio and signal-to-noise ratio, the catalog classified sources as point-like or extended, finding 8.4% to be extended. Using the same completeness and reliability assessment method as GLEAM-I, the results show 50% completeness at 25 mJy, 90% completeness at 50 mJy, and 99.994% reliability [25].

The GLEAM survey covers most of the southern sky, including many deep multi-wavelength fields such as Galaxy and Mass Assembly (GAMA), Chandra Deep Field South (CDFS), European Large Area ISO Survey-South 1 (ELAIS-S1), and two MWA fields dedicated to detecting the global EoR signal: EoR0 (centered at 00h, 27°) and EoR1 (04h, 30°). The GLEAM catalogs not only contain extensive information for studying southern sky extragalactic radio sources —such as flux density distributions, spectral index distributions, completeness, and extended source distributions—but also serve as reliable flux calibration catalogs for other low-frequency southern sky observations, including EoR studies with MWA, PAPER, and the upcoming SKA telescope.

3.2 LoLSS

The LoLSS (LOFAR Low-frequency Sky Survey) is a northern sky survey project using LOFAR's low-band antennas in the 42–66 MHz frequency range, aiming to cover the entire northern sky with 15 resolution and 1 mJy sensitivity. LoLSS-DR1 is the first data release, covering 740 square degrees [109] and containing 25,247 radio point sources. Sources were extracted from interferometric images using Python Blob Detection and Source Finder (PyBDSF) [110], with source type results provided: "S"for isolated point sources, "C"for large complex sources, and "M" for sources with multiple radio emission components. Completeness was assessed by adding 6,000 simulated sources with ionospheric effects and detecting them with PyBDSF, repeated 50 times. The final completeness simulation achieves 50% at 17 mJy and 90% at 40 mJy. Reliability was evaluated by inverting mosaic image pixel values (negative pixels from noise and artifacts become positive, while positive source pixels become negative) and extracting sources with the same method, detecting 1,055 sources and concluding that 4% of sources in LoLSS-DR1 are spurious.

The unique combination of high angular resolution and sensitivity in LoLSS-DR1 or the future complete LoLSS catalog will enable studies of "fossil" steep-spectrum sources, crucial for understanding the properties, evolution, and life-cycles of synchrotron-dominated radio sources. The LoLSS catalog can also investigate processes that modify the power-law synchrotron spectrum at very low frequencies (42–66 MHz), providing new information on processes such as ionized gas absorption and synchrotron self-absorption. Combining LoLSS with LoTSS will produce a unique dataset beneficial for low-frequency radio source research. Finally, long-term ionospheric observations at very low frequencies will help constrain and improve future ionospheric models.

3.3 LoTSS

The LoTSS-DR1 catalog is the first low-frequency point source survey catalog from LOFAR' s LoTSS project, covering 424 square degrees from right ascension 10h45m00s to 15h30m00s and declination 45°00 00 to 57°00 00 , detecting 325,694 radio point sources [27] in the 120–168 MHz frequency range. Completeness simulations (inserting simulated sources and extracting them with PyBDSF) show 65% completeness at 0.18 mJy, 90% at 0.35 mJy, and 95% at 0.45 mJy [27]. The catalog was cross-matched with optical data from Pan-STARRS [111, 112] and mid-infrared photometry from the Wide-field Infrared Survey Explorer (WISE) mission [113], with 73% of radio point sources having matches in both Pan-STARRS and WISE [114]. A novel hybrid photometric redshift method was used to estimate redshifts for each source [115], providing redshift information for most sources in the catalog.

The LoTSS-DR2 catalog is the second data release from the LoTSS project [116], covering two regions centered at (12h45m, +44°30) and (1h00m, +28°00) with areas of 4,178 and 1,457 square degrees respectively, totaling 5,635 square

degrees. It observed 4,396,228 radio point sources, most of which were not previously detected in radio surveys. Completeness simulations using simulated sources show 50% completeness at 0.34 mJy, 90% at 0.8 mJy, and 95% at 1.1 mJy. The catalog also provides PyBDSF source type fitting results.

The LoTSS catalogs contain extensive information on flux density distributions, spectral index distributions, and source counts at low frequencies, and their high angular resolution and wide coverage make them valuable references for flux calibration in other northern low-frequency observations.

The LoTSS-DP-DR1 extragalactic point source catalog was released from LOFAR deep field observations, covering 25.6 square degrees in three small fields: ELAIS-N1, Boötes, and Lockman Hole. It detects radio sources up to redshift 7 with a flux limit of 0.003 mJy, containing 81,951 radio point sources with 150 MHz flux densities, redshifts, source classifications, star formation rates, and stellar masses—making it the largest deep-field catalog with radio point source classifications to date [31].

This catalog was obtained by cross-matching the initial LoTSS deep field catalog of 7.2×10^6 radio point sources with optical, mid-infrared, and far-infrared observations [29], using four spectral energy distribution fitting codes (MAGPHYS [117], BAGPIPES [118, 119], CIGALE [120–122], AGNFITTER [123]) to determine whether sources are AGN-dominated and to estimate stellar masses and star formation rates.

For source classification, since radio brightness in star-forming galaxies is tightly correlated with star formation rate, sources with radio brightness significantly deviating from SFR predictions are classified as AGN [78, 124, 125]. The predicted relationship between star formation rate and radio luminosity is:

$$\log(L_{150\mathrm{MHz}}) = 22.24 + 1.08\log(\mathrm{SFR})$$

where L_{150}MHz (in $\mathrm{W \cdot Hz^{-1}}$) is the predicted radio luminosity and SFR (in $\mathrm{M_\odot \cdot yr^{-1}}$) is the star formation rate. If the observed radio luminosity exceeds the SFR-predicted value by 0.7 dex, the source is considered radio-excess. However, since the dispersion between SFR and observed radio luminosity for Boötes field sources increases with redshift, the radio-excess criterion for this field was modified to (0.7 + 0.1z) [31] to ensure consistent classification. Sources were then classified as: high-excitation radio galaxies (AGN mode + radio-excess), low-excitation radio galaxies (non-AGN mode + radio-excess), radio-quiet AGN (AGN mode + non-excess), and star-forming galaxies (non-AGN mode + non-excess) [31]. The distribution of different source types is shown in Table 3 , with star-forming galaxies being the majority (67.9%) and high-excitation radio galaxies the minority (2.1%).

Table 3 Distribution of different radio point source types in the LoTSS-DP-DR1 extragalactic point source catalog

With its information on source classification, redshift, flux density, star formation rate, and stellar mass, this catalog is important for studying redshift distributions, flux distributions, SFR distributions, and luminosity functions of different source types [31, 126, 127]. The completeness for all source types is approximately 50% at 0.2 mJy [126, 127]; for high- and low-excitation radio galaxies, completeness exceeds 90% above 1.6 mJy [126]; for RQ-AGN and star-forming galaxies, completeness exceeds 90% above 0.63 mJy [127].

3.4 3CRR

The 3CRR (Revised Revised Third Cambridge Catalog of Radio Sources) low-frequency point source catalog is a bright source sample at 178 MHz, covering 13,886 square degrees with 178 sources and a flux limit of 10.9 Jy, achieving over 96% completeness overall [34]. Ninety-six percent of sources have optical counterparts, and based on optical spectral information, sources are classified as radio galaxies or quasars (71% galaxies, 25% quasars). The catalog also estimates redshifts for all sources from optical spectra and classifies them as FRI or FRII based on morphology. Sources with radio emission concentrated around the optical identification center are FRI, while those with maximum brightness in radio lobes distant from the center are "C" if dominated by unresolvable components at > 1 GHz. The catalog also fits spectral indices for all sources from 178–750 MHz and includes B, V, and R band magnitudes.

The 3CRR catalog contains numerous bright sources with optical spectra, classifications, redshifts, and multi-band magnitudes, making it valuable for bright source studies. Some bright sources with stable flux densities are frequently used as calibration sources, such as 3C48, 3C138, 3C147, and 3C286.

3.5 7CRS

The 7CRS (Seventh Cambridge Redshift Survey) catalog was observed with the Cambridge Low Frequency Synthesis Telescope (CLFST), divided into 7C-I, 7C-II, and 7C-III based on sky region, covering a total area of 0.022 steradians at 151 MHz with a flux limit of 0.5 Jy (1/20 of the 3CRR catalog) [128, 129]. Through extensive optical and near-infrared cross-matching, 130 sources were identified with redshift information for 90%, up to $z = 3.6$. The catalog provides K-band magnitudes and has been used to study the M_K–z relation, which is well described by $M\_K = 17.37 + 4.53 \log z - 0.31(\log z)^2$. There is a significant difference in K-band absolute magnitudes between 3CRR sources and weaker 7CRS sources at all redshifts, possibly due to black hole mass effects [130].

3.6 21CMA-NCP

The 21CMA-NCP (21 CentiMeter Array North Celestial Pole) low-frequency point source catalog was obtained by the 21CMA interferometric array located in the Tianshan Mountains of Xinjiang, China, covering the north celestial pole at 75–175 MHz with 12.5 MHz bandwidth, detecting 624 sources. The spectral

index distribution peaks at -0.8, as expected, with steeper sources appearing at higher frequencies. Source count statistics for all frequency bands are shown in Figures 3 [FIGURE:3] and 4 [FIGURE:4]. Completeness simulations for different frequency bands show completeness dropping rapidly below 0.1 Jy, reaching 50% at 0.2 Jy and 100% above 1 Jy at higher frequencies [32].

3.7 VLSSr

The VLSSr (VLA Low-frequency Sky Survey Redux) extragalactic point source catalog was obtained from the Very Large Array (VLA) low-frequency sky survey [106], covering approximately 30,530 square degrees at 74 MHz with a flux limit of 0.39 Jy, totaling 92,964 sources. To assess source reality, the catalog was cross-matched with the 1.4 GHz NVSS point source catalog [131]. Sources without a second component within 120 were defined as isolated and cross-matched with NVSS, finding 2.2% of isolated sources without matches, considered spurious detections. The catalog also statistically analyzed the 74–1400 MHz spectral index distribution, with a median value of -0.82, and performed source count statistics but no completeness survey.

Covering nearly the entire sky north of declination -30°, this catalog is one of the most extensive for low-frequency extragalactic point source studies. Despite limitations, it serves as an important low-frequency reference for multi-wavelength studies of extragalactic sources [132–134], provides low-frequency comparison points for other surveys [135], and offers a global sky model for initial calibration of other low-frequency instruments and arrays [136, 137].

3.8 T-RaMiSu

The T-RaMiSu (Two-meter Radio Mini Survey) low-frequency extragalactic point source catalog was obtained by the Giant Metrewave Radio Telescope (GMRT) observing the Boötes field at 153 MHz [105], covering 30 square degrees with a flux limit of 4.1 mJy, totaling 1,289 sources. Monte Carlo simulations were used to model the relationship between integrated-to-peak flux density ratio and signal-to-noise ratio, classifying sources as extended or point-like and providing semi-major axes and position angles for extended sources. Completeness was assessed by adding simulated sources of different flux densities and searching with PyBDSF. Both completeness and reliability increase with flux density, reaching 95% and 92% respectively at 14 mJy.

The catalog provides source count statistics for flux densities of 15 mJy–7 Jy and spectral index statistics for sources > 0.1 Jy, with mean spectral indices of -0.25 for 153–1400 MHz and -0.2 for 153–327 MHz.

3.9 GLEAM-6dFGS

The GLEAM-6dFGS low-frequency extragalactic point source catalog was obtained by cross-matching the GLEAM-III catalog with the Six-degree Field Galaxy Survey (6dFGS) [33], covering approximately 16,700 square degrees at

72–231 MHz with 1,590 sources. The sample has a median redshift of 0.064 and maximum redshift of 0.283. Based on optical spectra, sources are classified as AGN (73%) or star-forming galaxies (27%). The catalog studied spectral index distributions for 76–227 MHz and 843–1400 MHz, finding median spectral indices of -0.704 ± 0.011 and -0.600 ± 0.010 for AGN, and -0.596 ± 0.015 and -0.650 ± 0.010 for star-forming galaxies. The overall catalog completeness is 95%.

The catalog has been used to fit local luminosity functions for radio point sources in the range 21.8–27.2 $\mathrm{W \cdot Hz^{-1}}$ [33]. The AGN luminosity function model is:

$$\Phi_{\mathrm{AGN}}(L) = \frac{C}{(L/L_\star)^\alpha + (L/L_\star)^\beta}$$

with characteristic luminosity $\mathrm{L\_} = 10^{25.76}$ $\mathrm{W \cdot Hz^{-1}}$, $\alpha = 1.76$, $\beta = 0.49$, and $\mathrm{C} = 10^{-6.13}$ $\mathrm{mag^{-1} \cdot Mpc^{-3}}$ [33].

The star-forming galaxy luminosity function model is:

$$\Phi_{\mathrm{SFG}}(L) = C \log\left(1 + \frac{L}{L_\star}\right) \exp\left[-\frac{1}{2\sigma^2} \log^2\left(1 + \frac{L}{L_\star}\right)\right]$$

with $\mathrm{C} = 10^{-2.84}$ $\mathrm{mag^{-1} \cdot Mpc^{-3}}$, $\mathrm{L\_} = 10^{21.06}$ $\mathrm{W \cdot Hz^{-1}}$, $\alpha = 0.68$, and $\sigma = 0.66$.

By matching GLEAM-III with 6dFGS to classify sources and fitting luminosity functions for both types, the catalog provides low-frequency (200 MHz) luminosity function models for AGN and star-forming galaxies, important for studying luminosity functions, redshift distributions, and spectral index distributions.

4 Radio Point Source Simulation Catalogs

Currently, the main radio point source simulation software includes T-RECS and SKADS. Compared to observations, simulated catalogs can cover larger sky areas, reach higher redshifts, and probe lower flux limits. They can be used to evaluate survey completeness or predict the number of sources to be observed in future surveys, and provide a method for studying extragalactic point source foregrounds for EoR signals.

Extragalactic point source simulation software has applications in multiple research areas. Recent work has used simulations to evaluate cosmic variance [138]; assess the number of sources detectable by SKA-VLBI interferometric arrays within specific beams and flux density levels, finding it feasible to locate multiple in-beam calibrators at L-band [139]; generate point source catalogs as training datasets for deep learning galaxy-finding software YOLO-CIANNA and for machine learning codes determining source count-flux density relationships

[140, 141]; study extragalactic point source clustering [101]; investigate the impact of peaked-spectrum extragalactic point sources on foreground removal and EoR signal extraction [142]; and evaluate the completeness of observed extragalactic point source catalogs [143].

4.1 SKADS

SKADS is a semi-empirical radio point source simulation software [40, 41]. "Semi-empirical" means simulated sources are extrapolated from observed radio point source luminosity functions [67, 144, 145], primarily modeling the large-scale cosmic distribution of radio sources. SKADS catalogs have the following characteristics: $20° \times 20°$ sky coverage, redshift up to 20, containing 320 million sources; flux limits of 10 nJy at 151 MHz, 610 MHz, 1.4 GHz, 4.86 GHz, and 18 GHz.

For source classification, SKADS divides simulated sources into radio-quiet AGN, radio-loud AGN, and star-forming galaxies. Radio-loud AGN are further divided into FRI and FRII based on morphological components, while star-forming galaxies are divided into normal galaxies and brighter, smaller starburst galaxies. The number, redshift distribution, and flux distribution of different source types are calculated from corresponding luminosity functions. Table 4 shows the numbers of different source types [40].

Table 4 Number of sources in each subclass in SKADS simulated $20° \times 20°$ continuous radio sky

Regarding source morphology, for radio-loud AGN, SKADS models FRI sources as a point core plus two coaxial elliptical lobes with uniform surface brightness based on FRI flux distributions; FRII sources are modeled as a point core, two elliptical lobes, and two hotspots. Component flux distributions are determined by the core-to-lobe ratio and jet Lorentz factor, with jet orientation angles set to random distributions. Other radio point sources and FRI/FRII cores are modeled as ellipses [146, 147] with parameters defined by major and minor axes in arcseconds.

For modeling large-scale cosmic distribution, source clustering is essential as it affects the power spectrum. SKADS combines radio point sources with a large-scale clustering underlying dark matter density field, using different matching patterns for different source types to obtain clustering effects [148–151].

SKADS extragalactic point source catalogs include clustering effects and have source count results at various frequencies that match observations well. Although observations indicate that SKADS underestimates the number of bright sources > 0.15 mJy at redshifts > 2 [127], it remains significant for predicting future observations and radio point source research in terms of flux distribution, source type numbers, and completeness studies.

4.2 T-RECS

T-RECS is a newer radio point source simulation software that models AGN and star-forming galaxies [42, 43]. Its main innovation compared to SKADS is modeling polarized emission from radio point sources. T-RECS covers 150 MHz–20 GHz, redshift up to 10, flux limit of 10 nJy, and provides 5° × 5° clustered radio point source sky catalogs.

T-RECS sets all AGN spectra as power-laws (S ^α), dividing them into flat-spectrum and steep-spectrum sources, with flat-spectrum sources further divided into flat-spectrum radio quasars and blazars. Steep-spectrum sources have spectral index -0.73 [43], while flat-spectrum sources have -0.1 [42]. Redshift-dependent luminosity function models are fitted and extrapolated using observational data [107] to obtain simulated sources down to 10 nJy flux limit and up to redshift 10. Polarized flux is calculated using polarization fraction models from relevant studies [152–154].

For star-forming galaxies, since radio emission is closely related to star formation rate, T-RECS uses redshift-evolving SFR functions to derive redshift-dependent luminosity functions [155–157], extrapolating to obtain simulated sources down to 10 nJy and up to redshift 10. The polarization model for star-forming galaxies assigns linear polarization fractions based on source inclination relationships [40].

For source sizes, T-RECS uses a pure geometric viewing angle distribution N( ) = sin for AGN intrinsic size models (same for star-forming galaxies) [102], then simulates intrinsic sizes using viewing angle size information from three extragalactic point source catalogs, repeated 1,000 times to obtain intrinsic size distributions [158–160]. This fitted intrinsic size distribution model is used to assign intrinsic sizes to AGN, which are then converted to angular sizes using redshift. For star-forming galaxies, the relationship between SFR and stellar mass [156] combined with the relationship between intrinsic size and stellar mass [161] yields the SFR–size relation, allowing assignment of intrinsic sizes based on SFR, then calculating angular sizes from redshift.

After obtaining sizes, T-RECS models source shapes: for steep-spectrum AGN, it models cores and two hotspots, using hotspot-to-core distance models to give angular distances [162], but does not provide flux distribution models for cores and hotspots. For star-forming galaxies, it assigns ellipticities based on galaxy ellipticity distribution models [163] and calculates major and minor angular axes from ellipticity, redshift, and intrinsic size.

T-RECS also models clustering using the P-Millennium dark matter halo simulation, which covers 5° × 5° and redshift 0–8. Clustering is obtained by matching dark matter halos with radio point sources by mass [157, 164].

T-RECS simulated catalogs contain not only flux information at different frequencies but also polarization, size, shape, and viewing angle information, enabling generation of field images using software like galsim [32]. Total and polar-

ized source counts in different frequency ranges are nearly consistent with real observations. However, observations also indicate that T-RECS underestimates the number of bright sources > 0.15 mJy at redshifts > 4 [127].

5 Summary and Outlook

Research on low-frequency extragalactic radio point sources helps understand how baryons drive and suppress star formation, deepening our understanding of galaxy formation and evolution. Since low-frequency radio point sources are important foreground contaminants for EoR signal detection, their study aids in foreground removal and suppression. Low-frequency radio point source observations are increasingly complete, particularly LOFAR deep fields providing high-redshift flux and redshift distribution information. This paper introduced key parameters of current low-frequency radio point source catalogs, including sky coverage, redshift range, frequency range, classification methods and results, and spectral indices. We also described major simulation software SKADS and T-RECS, including their modeling methods and catalog information.

Complete extragalactic point source catalogs have multiple applications in current astronomical research. They can be used to study galaxy clustering [101]; combined with cosmic microwave background lensing maps to constrain radio galaxy bias evolution and matter perturbation amplitude [165]; investigate cosmic variance and large-sample galaxy properties and their evolution [100]; study extragalactic point source size distributions [102]; obtain high-redshift bright radio source information from deep fields to study early universe conditions [166]; and search for sources with special properties through wide-area surveys [167]. Extragalactic point source simulation software and catalogs are also helpful for clustering studies and interferometric array calibration [138, 139], offering advantages over observed catalogs such as completeness, lower flux densities, and higher redshifts. They can serve as training sets for machine learning and deep learning related to point sources [140, 141] and evaluate extragalactic point source contamination of EoR signals [142].

Current low-frequency radio observations still lack measurements of point source polarization intensity. Since the spectral smoothness of radio point sources is affected by polarization leakage, obtaining relevant polarization leakage models would greatly benefit foreground removal. The world' s largest interferometric radio telescope, SKA, is under active construction. With its extremely high sensitivity and angular resolution, its observations will further test current models once operational.

References

[1] Miller N A, Bonzini M, Fomalont E B, et al. ApJS, 2013, 205: 13
[2] Barrett P E, Dieck C, Beasley A J, et al. AJ, 2017, 154: 252
[3] Malefahlo E, Santos M G, Jarvis M J, et al. MNRAS, 2020, 492: 5297
[4] Somalwar J J, Ravi V, Dong D, et al. ApJ, 2022, 929: 184

[5] Morales M F, Wyithe J S B. ARA&A, 2010, 48: 127
[6] Koopmans L, Pritchard J, Mellema G, et al. Advancing Astrophysics with the Square Kilometre Array(AASKA14). Italy: Sissa Medialab, 2015: 1
[7] Mellema G, Koopmans L V E, Abdalla F A, et al. Experimental Astronomy, 2013, 36: 235
[8] Mellema G, Koopmans L, Shukla H, et al. Advancing Astrophysics with the Square Kilometre Array (AASKA14). Italy: Sissa Medialab, 2015: 10
[9] Cassano R, Bernardi G, Brunetti G, et al. Advancing Astrophysics with the Square Kilometre Array (AASKA14). Italy: Sissa Medialab, 2015: 73
[10] Vazza F, Ferrari C, Bonafede A, et al. Advancing Astrophysics with the Square Kilometre Array (AASKA14). Italy: Sissa Medialab, 2015: 97
[11] Kale R, Dwarakanath K S, Vir Lal D, et al. Journal of Astrophysics and Astronomy, 2016, 37: 31
[12] Johnston-Hollitt M, Govoni F, Beck R, et al. Advancing Astrophysics with the Square Kilometre Array (AASKA14). Italy: Sissa Medialab, 2015: 92
[13] Roy S, Sur S, Subramanian K, et al. Journal of Astrophysics and Astronomy, 2016, 37: 42
[14] Van Eck C L, Haverkorn M, Alves M I R, et al. A&A, 2017, 597: A98
[15] Stappers B W, Hessels J W T, Alexov A, et al. A&A, 2011, 530: A80
[16] Fender R, Stewart A, Macquart J P, et al. Advancing Astrophysics with the Square Kilometre Array (AASKA14). Italy: Sissa Medialab, 2015: 51
[17] Padovani P. A&A Rev, 2016, 24: 13
[18] Shaver P A, Windhorst R A, Madau P, et al. A&A, 1999, 345: 380
[19] Murray S G, Trott C M, Jordan C H. ApJ, 2017, 845: 7
[20] Procopio P, Wayth R B, Line J, et al. PASA, 2017, 34: e033
[21] Bowman J D, Morales M F, Hewitt J N. ApJ, 2009, 695: 183
[22] Burke B F, Graham, Wilkinson P N. An introduction to radio astronomy, 4th edition. Cambridge: Cambridge University Press, 2019
[23] Hurley-Walker N, Callingham J R, Hancock P J, et al. MNRAS, 2017, 464: 1146
[24] Hurley-Walker N, Hancock P J, Franzen T M O, et al. PASA, 2019, 36: e047
[25] Franzen T M O, Hurley-Walker N, White S V, et al. PASA, 2021, 38: e014
[26] Shimwell T W, Röttgering H J A, Best P N, et al. A&A, 2017, 598: A104
[27] Shimwell T W, Tasse C, Hardcastle M J, et al. A&A, 2019, 622: A1
[28] Sabater J, Best P N, Tasse C, et al. A&A, 2021, 648: A2
[29] Kondapally R, Best P N, Hardcastle M J, et al. A&A, 2021, 648: A3
[30] Duncan K J, Kondapally R, Brown M J I, et al. A&A, 2021, 648: A4
[31] Best P N, Kondapally R, Williams W L, et al. MNRAS, 2023, 523: 1729
[32] Zheng Q, Wu X P, Johnston-Hollitt M, et al. ApJ, 2016, 832: 190
[33] Franzen T M O, Seymour N, Sadler E M, et al. PASA, 2021, 38: e041
[34] Laing R A, Riley J M, Longair M S. MNRAS, 1983, 204: 151
[35] Rawlings S, Eales S, Lacy M. MNRAS, 2001, 322: 523
[36] Lacy M, Riley J M, Waldram E M, et al. MNRAS, 1995, 276: 614
[37] Willott C J, Rawlings S, Blundell K M, et al. MNRAS, 1998, 300: 625
[38] Lacy M, Rawlings S, Hill G J, et al. MNRAS, 1999, 308: 1096

[39] Jarvis M J, Rawlings S, Eales S, et al. MNRAS, 2001, 326: 1585
[40] Wilman R J, Miller L, Jarvis M J, et al. MNRAS, 2008, 388: 1335
[41] Wilman R J, Jarvis M J, Mauch T, et al. MNRAS, 2010, 405: 447
[42] Bonaldi A, Bonato M, Galluzzi V, et al. MNRAS, 2019, 482: 2
[43] Bonaldi A, Hartley P, Ronconi T, et al. MNRAS, 2023, 524: 993
[44] Soderberg A M, Chevalier R A, Kulkarni S R, et al. ApJ, 2006, 651: 1005
[45] Condon J J. ARA&A, 1992, 30: 575
[46] Ginzburg V L, Syrovatskii S I. ARA&A, 1969, 7: 375
[47] Padovani P, Alexander D M, Assef R J, et al. A&A Rev, 2017, 25: 2
[48] Miley G. ARA&A, 1980, 18: 165
[49] Padovani P, Bonzini M, Kellermann K I, et al. MNRAS, 2015, 452: 1263
[50] Sargent M T, Schinnerer E, Murphy E, et al. ApJS, 2010, 186: 341
[51] Bonzini M, Mainieri V, Padovani P, et al. MNRAS, 2015, 453: 1079
[52] Noeske K G, Weiner B J, Faber S M, et al. ApJL, 2007, 660: L43
[53] Elbaz D, Daddi E, Le Borgne D, et al. A&A, 2007, 468: 33
[54] Daddi E, Dickinson M, Morrison G, et al. ApJ, 2007, 670: 156
[55] Heckman T M, Best P N. ARA&A, 2014, 52: 589
[56] Antonucci R. Astronomical and Astrophysical Transactions, 2012, 27: 557
[57] Narayan R, Yi I. ApJL, 1994, 428: L13
[58] Narayan R, Yi I. ApJ, 1995, 452: 710
[59] Narayan R. Ap&SS, 2005, 300: 177
[60] Quataert E. Probing the Physics of Active Galactic Nuclei: Vol. 224. San Francisco: ASP, 2001: 71
[61] Ho L C. ARA&A, 2008, 46: 475
[62] Fanaroff B L, Riley J M. MNRAS, 1974, 167: 31P
[63] Gendre M A, Best P N, Wall J V, et al. MNRAS, 2013, 430: 3086
[64] Baldi R D, Capetti A, Giovannini G. A&A, 2015, 576: A38
[65] Wall J V. The Observatory, 1975, 95: 196
[66] Peacock J A, Gull S F. MNRAS, 1981, 196: 611
[67] Willott C J, Rawlings S, Blundell K M, et al. MNRAS, 2001, 322: 536
[68] Kimball A E, Ivezić Ž. AJ, 2008, 136: 684
[69] Massardi M, Ekers R D, Murphy T, et al. MNRAS, 2011, 412: 318
[70] Kellermann K I, Condon J J, Kimball A E, et al. ApJ, 2016, 831: 168
[71] Padovani P, Petropoulou M, Giommi P, et al. MNRAS, 2015, 452: 1877
[72] Mancuso C, Lapi A, Prandoni I, et al. ApJ, 2017, 842: 95
[73] White S V, Jarvis M J, Kalfountzou E, et al. MNRAS, 2017, 468: 217
[74] Peacock J A, Miller L, Longair M S. MNRAS, 1986, 218: 265
[75] Zakamska N L, Lampayan K, Petric A, et al. MNRAS, 2016, 455: 4191
[76] Schmidt M. ApJ, 1970, 162: 371
[77] Padovani P. Nature Astronomy, 2017, 1: 0194
[78] Delvecchio I, Smolčić V, Zamorani G, et al. A&A, 2017, 602: A3
[79] Ceraj L, Smolčić V, Delvecchio I, et al. A&A, 2018, 620: A192
[80] Kimball A E, Ivezić Ž, Wiita P J, et al. AJ, 2011, 141: 182
[81] Condon J J, Kellermann K I, Kimball A E, et al. ApJ, 2013, 768: 37
[82] White S V, Jarvis M J, Häußler B, et al. MNRAS, 2015, 448: 2665
[83] Sopp H M, Alexander P. MNRAS, 1991, 251: 14P

[84] Ho L C, Ulvestad J S. ApJS, 2001, 133: 77
[85] Laor A, Behar E. MNRAS, 2008, 390: 847
[86] Wang J M. ApJL, 2008, 682: L81
[87] Hine R G, Longair M S. MNRAS, 1979, 188: 111
[88] Tadhunter C N, Morganti R, Robinson A, et al. MNRAS, 1998, 298: 1035
[89] Laing R A, Jenkins C R, Wall J V, et al. The Physics of Active Galaxies: Vol. 54. San Francisco: ASP, 1994: 201
[90] Kewley L J, Groves B, Kauffmann G, et al. MNRAS, 2006, 372: 961
[91] Buttiglione S, Capetti A, Celotti A, et al. A&A, 2009, 495: 1033
[92] Buttiglione S, Capetti A, Celotti A, et al. A&A, 2010, 509: A6
[93] Shakura N I, Sunyaev R A. A&A, 1973, 24: 337
[94] McAlpine K, Jarvis M J, Bonfield D G. MNRAS, 2013, 436: 1084
[95] Best P N, Heckman T M. MNRAS, 2012, 421: 1569
[96] Hardcastle M J, Evans D A, Croston J H. MNRAS, 2006, 370: 1893
[97] Ogle P, Whysong D, Antonucci R. ApJ, 2006, 647: 161
[98] Chiaberge M, Macchetto F D, Sparks W B, et al. ApJ, 2002, 571: 247
[99] Evans D A, Worrall D M, Hardcastle M J, et al. ApJ, 2006, 642: 96
[100] Kochanek C S, Eisenstein D J, Cool R J, et al. ApJS, 2012, 200: 8
[101] Hale C L, Schwarz D J, Best P N, et al. MNRAS, 2024, 527: 6540
[102] DiPompeo M A, Runnoe J C, Myers A D, et al. ApJ, 2013, 774: 24
[103] Intema H T, van Weeren R J, Röttgering H J A, et al. A&A, 2011, 535: A38
[104] Ghosh A, Prasad J, Bharadwaj S, et al. MNRAS, 2012, 426: 3295
[105] Williams W L, Intema H T, Röttgering H J A. A&A, 2013, 549: A55
[106] Lane W M, Cotton W D, van Velzen S, et al. MNRAS, 2014, 440: 327
[107] Massardi M, Bonaldi A, Negrello M, et al. MNRAS, 2010, 404: 532
[108] Offringa A R, McKinley B, Hurley-Walker N, et al. MNRAS, 2014, 444: 606
[109] de Gasperin F, Williams W L, Best P, et al. A&A, 2021, 648: A104
[110] Mohan N, Rafferty D. https://ui.adsabs.harvard.edu/abs/2015ascl.soft02007M, 2015
[111] Kaiser N, Aussel H, Burke B E, et al. SPIE, 2002, 4836: 154
[112] Kaiser N, Burgett W, Chambers K, et al. SPIE, 2010, 7733: 77330E
[113] Wright E L, Eisenhardt P R M, Mainzer A K, et al. AJ, 2010, 140: 1868
[114] Williams W L, Hardcastle M J, Best P N, et al. A&A, 2019, 622: A2
[115] Duncan K J, Sabater J, Röttgering H J A, et al. A&A, 2019, 622: A3
[116] Shimwell T W, Hardcastle M J, Tasse C, et al. A&A, 2022, 659: A1
[117] da Cunha E, Charlot S, Elbaz D. MNRAS, 2008, 388: 1595
[118] Carnall A C, McLure R J, Dunlop J S, et al. MNRAS, 2018, 480: 4379
[119] Carnall A C, Leja J, Johnson B D, et al. ApJ, 2019, 873: 44
[120] Burgarella D, Buat V, Iglesias-Páramo J. MNRAS, 2005, 360: 1413
[121] Noll S, Burgarella D, Giovannoli E, et al. A&A, 2009, 507: 1793
[122] Boquien M, Burgarella D, Roehlly Y, et al. A&A, 2019, 622: A103
[123] Calistro Rivera G, Lusso E, Hennawi J F, et al. ApJ, 2016, 833: 98
[124] Williams W L, Calistro Rivera G, Best P N, et al. MNRAS, 2018, 475: 3429

[125] Whittam I H, Jarvis M J, Hale C L, et al. MNRAS, 2022, 516: 245
[126] Kondapally R, Best P N, Cochrane R K, et al. MNRAS, 2022, 513: 3742
[127] Cochrane R K, Kondapally R, Best P N, et al. MNRAS, 2023, 523: 6082
[128] Willott C J, Rawlings S, Blundell K M, et al. MNRAS, 2002, 335: 1120
[129] Lacy M, Bunker A J, Ridgway S E. AJ, 2000, 120: 68
[130] Willott C J, Rawlings S, Jarvis M J, et al. MNRAS, 2003, 339: 173
[131] Condon J J, Cotton W D, Greisen E W, et al. AJ, 1998, 115: 1693
[132] Brunetti G, Giacintucci S, Cassano R, et al. Nature, 2008, 455: 944
[133] Kothes R, Landecker T L, Reich W, et al. ApJ, 2008, 687: 516
[134] Argo M K, Paragi Z, Rottgering H, et al. MNRAS, 2013, 431: L58
[135] Bernardi G, Greenhill L J, Mitchell D A, et al. ApJ, 2013, 771: 105
[136] van Haarlem M P, Wise M W, Gunst A W, et al. A&A, 2013, 556: A2
[137] Taylor G B, Ellingson S W, Kassim N E, et al. Journal of Astronomical Instrumentation, 2012, 1: 1250004
[138] Matthews A M, Kelson D D, Newman A B, et al. ApJ, 2024, 966: 194
[139] Li Y, Xu Y, Li J, et al. arXiv e-prints, 2024: arXiv:2404.14663
[140] Cornu D, Salomé P, Semelin B, et al. A&A, 2024, 690: A211
[141] Todarello E, Scaffidi A, Regis M, et al. JCAP, 2024, 2024: 062
[142] He M, Zheng Q, Guo Q, et al. MNRAS, 2024, 529: 3140
[143] Duchesne S W, Grundy J A, Heald G H, et al. PASA, 2024, 41: e003
[144] Ueda Y, Akiyama M, Ohta K, et al. ApJ, 2003, 598: 886
[145] Yun M S, Reddy N A, Condon J J. ApJ, 2001, 554: 803
[146] Blundell K M, Rawlings S, Willott C J. AJ, 1999, 117: 677
[147] Broeils A H, Rhee M H. A&A, 1997, 324: 877
[148] Croom S M, Boyle B J, Shanks T, et al. MNRAS, 2005, 356: 415
[149] Overzier R A, Röttgering H J A, Rengelink R B, et al. A&A, 2003, 405: 53
[150] Farrah D, Lonsdale C J, Borys C, et al. ApJL, 2006, 641: L17
[151] Swinbank A M, Chapman S C, Smail I, et al. MNRAS, 2006, 371: 465
[152] Hales C A, Norris R P, Gaensler B M, et al. MNRAS, 2014, 440: 3113
[153] Galluzzi V, Massardi M, Bonaldi A, et al. MNRAS, 2018, 475: 1306
[154] Murphy T, Sadler E M, Ekers R D, et al. MNRAS, 2010, 402: 2403
[155] Cai Z Y, Lapi A, Xia J Q, et al. ApJ, 2013, 768: 21
[156] Mancuso C, Lapi A, Cai Z Y, et al. ApJ, 2015, 810: 72
[157] Aversa R, Lapi A, de Zotti G, et al. ApJ, 2015, 810: 74
[158] Barthel P D. ApJ, 1989, 336: 606
[159] Singal A K, Laxmi Singh R. ApJ, 2013, 766: 37
[160] Boroson T A. American Astronomical Society Meeting Abstracts: Vol. 217. America: AAS, 2011: 142.22
[161] Shen S, Mo H J, White S D M, et al. MNRAS, 2003, 343: 978
[162] Lin Y T, Shen Y, Strauss M A, et al. ApJ, 2010, 723: 1119
[163] Tunbridge B, Harrison I, Brown M L. MNRAS, 2016, 463: 3339
[164] Janssen R M J, Röttgering H J A, Best P N, et al. A&A, 2012, 541: A62
[165] Nakoneczny S J, Alonso D, Bilicki M, et al. A&A, 2024, 681: A105
[166] Miley G, De Breuck C. A&A Rev, 2008, 15: 67
[167] Fan X, SDSS Collaboration. Next Generation Wide-Field Multi-Object

Spectroscopy: Vol. 280. San Francisco: ASP, 2002: 43